RSC Advances

PAPER

View Article Online
View Journal | View Issue

Cite this: *RSC Adv.*, 2019, **9**, 32121

Influence of nitrogen/phosphorus-doped carbon dots on polyamide thin film membranes for water vapor/N_2 mixture gas separation†

Yogita M. Shirke,[ab] Ali M. Abou-Elanwar,[abc] Won-Kil Choi,[a] Hyojin Lee,[a] Seong Uk Hong,[d] Hyung Keun Lee[a] and Jae-Deok Jeon *[a]

Nanoparticles have been attracting attention because they can significantly improve the performance of membranes when added in small amounts. In this study, the effect of polyamide membranes incorporating hydrophilic nitrogen/phosphorus-doped carbon dots (NP-CDs) to enhance water vapor/N_2 separation has been investigated. NP-CD nanoparticles with many hydrophilic functional groups are synthesized from chitosan by a one-pot green method and introduced to the surface of the polysulfone (PSf) substrates by interfacial polymerization reaction. The mean particle diameter of NP-CDs, estimated from transmission electron microscopy images, is 2.6 nm. By adding NP-CDs (0–1.5 wt%) to the polyamide layer, the contact angles of the membranes dramatically decreased from 65° (PSf) to <9° (thin film nanocomposite (TFN)), which means that the TFN membranes become significantly hydrophilic. From the water vapor separation results, the addition of NP-CDs in the polyamide layer improves the water vapor permeance from 1511 (thin film composite (TFC) without nanoparticles) to 2448 GPU (TFN with 1.0 wt% NP-CD loading, CD-TFN(1.0)) and the water vapor/N_2 selectivity from 73 (TFC) to 854 (CD-TFN(1.0)). To our knowledge, this is the first study of highly functionalized NP-CD-incorporated polyamide membranes to enhance water vapor separation.

Received 13th August 2019
Accepted 18th September 2019

DOI: 10.1039/c9ra06300e

rsc.li/rsc-advances

Introduction

Currently, coal-fired power plants require a considerable amount of water for heat rejection, power augmentation, preparation of fuel, control of emissions, and cycle makeup.[1] It was reported that a typical 700 MW power plant in the U.S. releases 30 000 liter of water vapor in one minute.[2] Most power plants are thus in a state of water stress and their water use is considered to have significant ecosystem impacts. Recovering some water from the discharged water would be very helpful to address the issues of water scarcity and energy consumption. Many researchers have accordingly sought to solve this problem through various approaches, including a condenser approach,[3,4] a desiccant drying approach,[5–7] and a membrane system approach.[8–11] Compared to other approaches, membrane separation requires less energy consumption because no phase change takes place during the dehumidification process, except for pervaporation. In addition, a membrane separation system has advantages of a compact/simple modular design, a small footprint, and environmental friendliness,[12] and thus has been widely used in recent years for various industrial gas separation approaches such as dehumidification of flue gas,[13] natural gas,[14] and compressed air.[15] Among the various membranes, polymeric membranes are attractive because of their excellent separation performance and low cost. The polymeric membranes for water vapor separation are mostly thin film composites (TFC), which are modified by coating thin polyamide layers on the surface of microporous polymeric substrates, leading to high membrane performance. The polyamide layer is usually synthesized *via* interfacial polymerization (IP) of an aqueous monomer with amine groups and an organic monomer with acid chloride groups. However, despite the progress in TFC membranes with relatively high permeance and selectivity, in order to further improve their performance, new membrane materials are still needed.

The incorporation of nanoparticles into the polymeric membranes is actively being studied because nanoparticles contain hydrophilic groups that provide a high degree of permeation channels for increased membrane separation performance.[16,17] The binding affinity of the nanoparticles with the polymer matrix can be increased by the interaction and the formation of hydrogen bonds or coordinate bonds without any

[a]*Greenhouse Gas Research Laboratory, Korea Institute of Energy Research (KIER), 152 Gajeong-ro, Yuseong-gu, Daejeon 34129, Republic of Korea. E-mail: jdjun74@kier.re.kr*
[b]*Department of Advanced Energy and Technology Korea, University of Science and Technology (UST), 217 Gajeong-ro, Yuseong-gu, Daejeon 34113, Republic of Korea*
[c]*Chemical Engineering Pilot Plant Department, Engineering Research Division, National Research Centre, Cairo 12622, Egypt*
[d]*Department of Chemical and Biological Engineering, Hanbat National University, 125 Dongseodero, Yuseong-gu, Daejeon 34158, Republic of Korea*

† Electronic supplementary information (ESI) available. See DOI: 10.1039/c9ra06300e

kind of defects.[18] Moreover, the nanoparticles are frequently changed to achieve desired outcomes by surface modification and by varying the dominant lattice parameter or structure. However, the performance of TFN membranes is restricted by agglomeration of nanoparticles, which leads to uneven distribution in the membranes. In this manner, surface modification of the nanoparticles is required to improve the performance of TFN membranes including the high packing capacity, loading capability, and separation property.[19]

In previous work, they modified TiO_2 nanoparticles with a median diameter of 70 nm by introducing acidic groups (–COOH) and fabricated TFN membranes by introducing them on the surface of polymeric hollow fibers for gas separation.[20,21] From the results, it was confirmed that the performance of TFN membranes with more than 0.2 w/w% COOH–TiO_2 loading was gradually decreased due to agglomeration of the nanoparticles. Also, the introduction of –OH groups on the surface of silicon nanoparticles significantly increased the hydrophilicity of the TFN membranes and therefore improved the membranes separation performance.[22] In addition, TiO_2 nanoparticles larger than 50 nm caused more agglomeration problems, further deteriorating performance. Polyamide membranes with smaller size nanoparticles thus showed higher performance than those with larger particles because small-sized nanoparticles can be easily and extensively dispersed on the polyamide surface and provide larger surface area due to increased surface roughness.[19,23] Therefore, by increasing the amount of hydrophilic functional moieties of nanoparticles, decreasing the nanoparticle size, and improving the nanoparticle dispersability, it is easy to make TFN membranes with desired performance. Firstly used graphene oxide quantum dot (GOQD), a typical type of CQDs that generally have better crystallinity than their siblings, as a nanofiller for antifouling and chlorine resistance TFN reverse osmosis membranes,[24] Bai *et al.* fabricated novel TFN membranes consisting of GOQD for low-pressure nanofiltration through interfacial polymerization and high-flux and antifouling properties of the resulting membranes.[25] The effect of carbon dots (CDs) on polyamide TFN Reverse osmosis membranes was also systematically researched by Zhang *et al.*[26]

Carbon dots (CDs), which are very small particles (typically below 10 nm in size), are applied in more and more field such as bioimaging, photovoltaic devices, florescent probes and so on,[27] because they have many attractive qualities such as simple synthesis, low toxicity, and high water dispersability as well as photostability.[28,29] In addition, CD nanoparticles can contain various hydrophilic functional moieties such as hydroxyl, amino, carboxyl, carbonyl, and other oxygenous moieties on their surface by surface modification. For these reasons, incorporation of surface-modified CD nanoparticles on the polyamide layer can be a good approach not only for enhancing the hydrophilic property of the surface of the membrane but also for simultaneously increasing the surface roughness and density of the polyamide layer.

In this study, we propose a new approach of synthesizing nitrogen/phosphorus-doped carbon dots (NP-CDs) from chitosan by a one-pot green method in an aqueous medium without using any harsh acids at a relatively mild temperature. Compared with other chemicals, chitosan is characterized by low cost and abundant resources derived from chitin, which is a major component of shellfish, crabs, and so on. In addition, chitosan is a rich source of amino ($-NH_2$) and hydroxyl (–OH) functional groups. The prepared NP-CD nanoparticles are incorporated on TFN membranes *via* an interfacial interaction (IP) between a diethylenetriamine (DETA) as aqueous monomer and trimesoyl chloride (TMC) as organic monomer on the surface of porous hollow fiber substrates. The abundant hydrophilic functional groups of the NP-CD nanoparticles enhance the dispersability and binding affinity towards DETA molecules during the IP reaction, thereby leading to the production of a dense polyamide layer, which in role improves performance. The effect of the NP-CD nanoparticles on the PSf substrates and the performance of the TFN membranes is studied by various analysis techniques. There have been no reports to our knowledge on NP-CD-incorporated membranes for water vapor separation.

Experimental

Reagents and materials

Microporous polysulfone (PSf) hollow fibers were used as a substrate in TFN membranes. Diethylenetriamine (DETA, 99%) and trimesoyl chloride (TMC, 98%) were purchased from Sigma-Aldrich. Chitosan (Sigma-Aldrich) was used as a precursor to synthesize carbon dots. Potassium dihydrogen phosphate (KH_2PO_4), *n*-hexane, and ethanol were purchased from Duksan Pure Chemical (Korea).

Synthesis of NP-carbon dot nanoparticles

NP-CD nanoparticles were synthesized by acidic oxidation of chitosan using KH_2PO_4, as shown in Fig. 1. A 40 mL of deionized water was added to 1.0 g of chitosan and 1.9 g KH_2PO_4 and stirred continuously for 30 min. The solution was then transferred into a hydrothermal synthesis autoclave reactor with 50 mL capacity. The reactor was sealed tightly and put into oven at 180 °C for 12 h. The product was separated by centrifuging at 8340 revolutions for 20 min and separated through a 0.45 μm syringe filter. The golden yellow-colored supernatant was separated and lyophilized. The resulting product was dispersed in ethyl alcohol in order to remove salts, and then separated through a 0.22 μm PTFE syringe filter. The collected particles containing the solution were evaporated by using a rotary evaporation process, resulting in brown-colored NP-CDs. The formation mechanism of NP-CDs based on previous research on heterotopic NP-CDs from small molecules is hypothesized as follows first step includes the hydrolysis, drying out, and degradation of small molecules. Second step includes the polymerization process of the products and aromatization of the polymers. Third step includes the nucleation and development of carbon materials. Final step includes the oxidation of the developed carbon materials.[30,31]

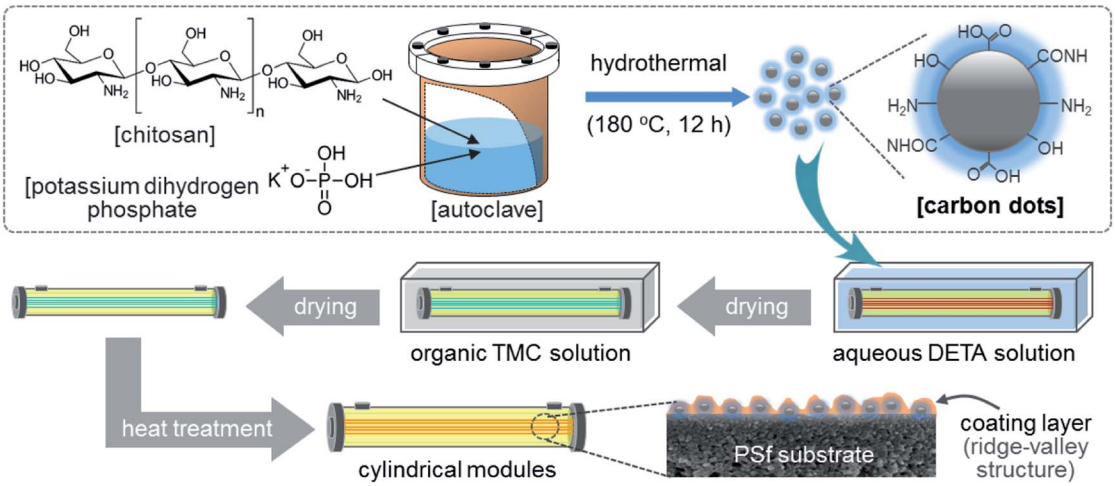

Fig. 1 Schematic illustration of synthesis of NP-CD nanoparticles and fabrication procedure of TFN membranes.

Preparation of TFN membranes

The NP-CD-incorporated polyamide layers were fabricated by using the IP method on the outer side of the PSf substrate. The cylindrical modules (30 cm length, five PSf hollow fibers) were first prepared. A known quantity of carbon dots was added to 2 wt% DETA in deionized water and sonicated for 15 min in an ultrasonic bath. PSf membranes were dipped in the aqueous DETA solution containing NP-CD nanoparticles for 20 min, followed by removal of excess solution and air drying for 10 min. Next, DETA-saturated membranes were dipped in 0.2 wt% TMC in *n*-hexane for 3 min, leading to the development of a thin polyamide layer with NP-CD nanoparticles. The membranes were then heated for 15 min at 75 °C for a further stabilization of the thin film layer. The fabrication procedure of the TFN membranes is illustrated in Fig. 1 and the control variables investigated in this study are presented in Table 1.

Characterization of NP-CDs and TFN membranes

The morphological and physicochemical properties of the NP-CD nanoparticles as well as TFN membranes containing these nanoparticles were measured by using different analytical characterization methods. The microscopic morphology and visual estimates of the particle size distribution of the NP-CD nanoparticles were carried out with high-resolution transmission electron microscopy (HRTEM) (Philips Tecnai 20). The size distribution of the NP-CD nanoparticles was statistically evaluated using image J software. A Zetasizer Nano ZS (Malvern Instruments Ltd.) detected the zeta potential of nanoparticles in an aqueous suspension. The various functional groups present on the surface of the NP-CD nanoparticles and composite membranes were investigated using Fourier transform infrared (FTIR) and attenuated total reflectance-FTIR spectroscopy (ART-FTIR) (ALPHA-P, Bruker Optik GmbH). The chemical composition of the NP-CD nanoparticles was investigated with X-ray photoelectron spectroscopy (XPS, MultiLab 2000) using a monochromatic Al Kα X-ray source. A UV-3600 spectrophotometer (Shimadzu) was used to investigate the optical features of the NP-CD nanoparticles. The typical powder X-ray diffraction (PXRD) patterns of the NP-CD nanoparticles were recorded on a Panalytical X'pert PRO powder X-ray diffractometer with Cu Kα radiation in the range $10^\circ \leq 2\theta \leq 80^\circ$. Scanning electron microscopy (SEM) (S4800-Hitachi) was performed to detect both the surface and cross-sectional morphologies of the membranes. The surface roughness parameters of the amide layers with and without NP-CD nanoparticles were investigated using the atomic force microscopy (AFM, Horiba Jovin Lee Bonn, Bruker). The water contact angle was measured to assess the hydrophilic nature of the membranes using a SEO Phoenix 300 plus instrument at room

Table 1 Coating conditions of TFC and TFN membranes[a]

Membrane code	DETA (wt%)	TMC (wt%)	NP-CD (wt%)	Reaction time (min)
DT-TFC	2	0.2	0	3
CD-TFN(0.1)	2	0.2	0.1	3
CD-TFN(0.2)	2	0.2	0.2	3
CD-TFN(0.5)	2	0.2	0.5	3
CD-TFN(1.0)	2	0.2	1.0	3
CD-TFN(1.5)	2	0.2	1.5	3

[a] NP-CD loading was taken with respect to DETA concentration.

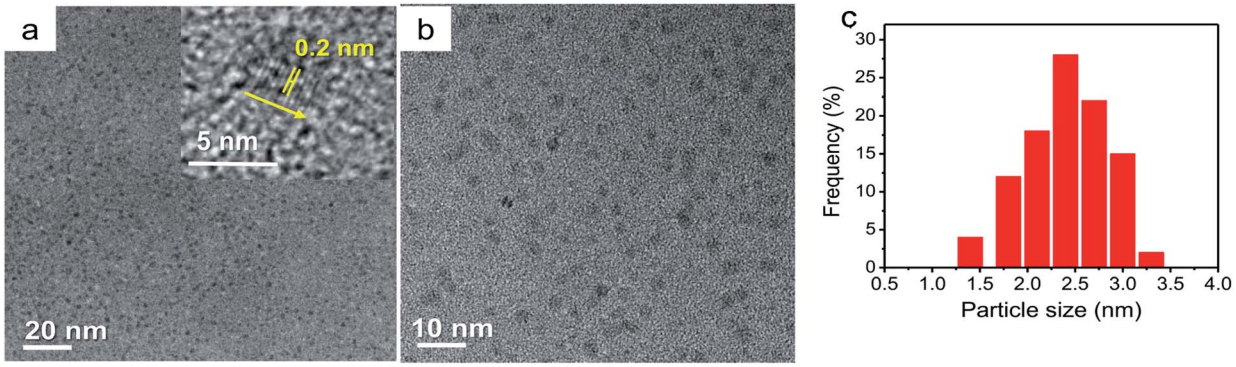

Fig. 2 (a and b) HRTEM images of NP-CDs (c) particle size distribution of NP-CD nanoparticles.

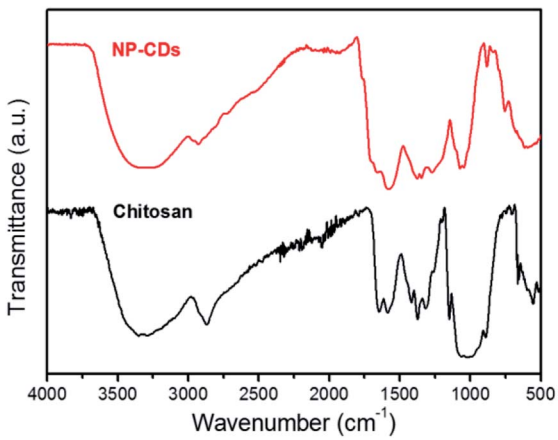

Fig. 3 FT-IR spectra of NP-CD nanoparticles and pure chitosan.

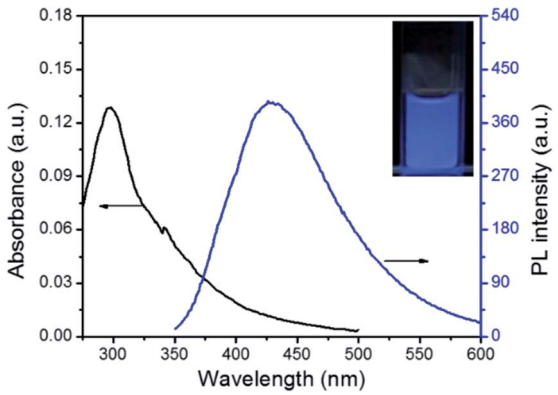

Fig. 5 UV-vis spectra (black line) and photo-luminesce spectra (blue line) of the NP-CDs in dispersion solution. Inset: the photograph of NP-CD nanoparticles at 365 nm wavelength.

temperature and a normal air atmosphere. The tests were conducted five times to ensure the reliability of the results and the average contact angle values were examined.

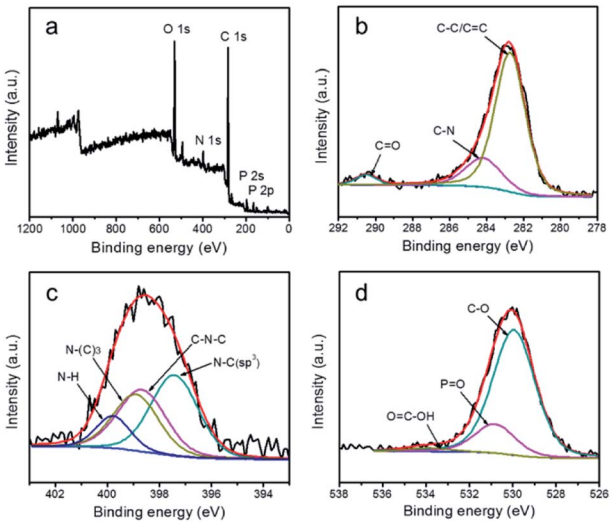

Fig. 4 (a) The XPS survey spectrum and high resolution (b) C 1s, (c) N 1s, and (d) O 2s lines XPS spectra of NP-CD nanoparticles.

Water vapor/N_2 permeation study

The separation performance of a water vapor/N_2 mixture gas was investigated using the device, illustrated in Fig. S1.† The gas separation setup system was maintained at a pressure of 3 bar with feed flow rate of 1000 mL min^{-1}. The cylindrical modules

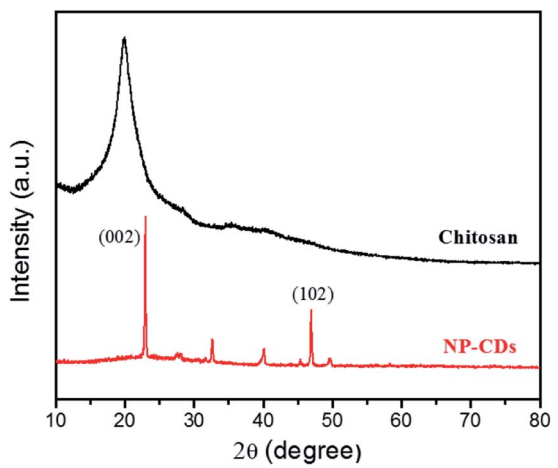

Fig. 6 XRD patterns of chitosan (black line) and NP-CDs (red line).

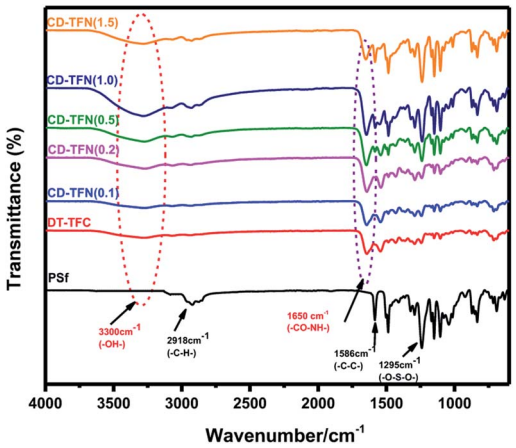

Fig. 7 ATR-FTIR spectra of PSf substrate, TFC, and TFN membranes.

with hollow fiber membranes were kept inside an oven with fixed temperature of 30 °C. Vaisala HMT334 humidity and temperature transmitters, which have relative humidity (RH) and temperature accuracies of ±1.0% (0–90% RH) and ±0.2 °C, respectively, were used to measure the change in the relative humidity and temperature after feed flow passes through the membranes. The following equation was used to evaluate the flow rate of water vapor in this study:

$$Q_{\text{vapor}} = \frac{Q_{N_2}\gamma_{H_2O}V_m}{M_{w,H_2O}} \quad (1)$$

standard flow rate of water vapor, the flow rate of the gas, and molar volume of water vapor at standard pressure and temperature conditions (22.4 L mol^{-1}) and the molar mass of water (18 g mol^{-1}), respectively. The water vapor flux, J_{H_2O} (cm^3 (STP) cm^{-2} s^{-1}), was estimated *via* the following equation:

$$J_{H_2O} = \frac{Q_{\text{vapor,p}}}{A} \quad (2)$$

where $Q_{\text{vapor,p}}$ (cm^3 (STP) s^{-1}) is the permeate flow rate of the water vapor and A (cm^2) is the effective area of the membrane.

The membrane water vapor permeance, P_{H_2O} (GPU), was determined from ΔP_{H_2O}, which represents the partial pressure of water vapor, as follows:

$$P_{H_2O} = \frac{J_{H_2O}}{\Delta P_{H_2O}} \quad (3)$$

The membranes selectivity, α, was calculated by using the following equation:

$$\alpha = \frac{P_{H_2O}}{P_{N_2}} \quad (4)$$

where P_{N_2} referred to the nitrogen gas permeance.

Results and discussion

Characterization of NP-CD nanoparticles

Particle size is an important parameter in materials science and technology because particles with small size can have a very large surface area to volume ratios. Therefore, it is worthwhile to synthesize nano-sized particles and measure their size and size distribution. The crystalline size and the size distribution of the as-prepared NP-CD nanoparticles studied by HRTEM are shown in Fig. 2. From the HRTEM images, it was confirmed that the NP-CD nanoparticles were uniformly dispersed without apparent aggregation and all of them were spherical in shape. The HRTEM image of a single particle (Fig. 2b) showed a crystalline nature with a lattice spacing of approximately 0.2 nm, which is well matched with the (102) crystal plane of graphitic carbon.[32,33] In addition, the particle size distribution histogram (Fig. 2c) was obtained by counting more than 100 particles. The

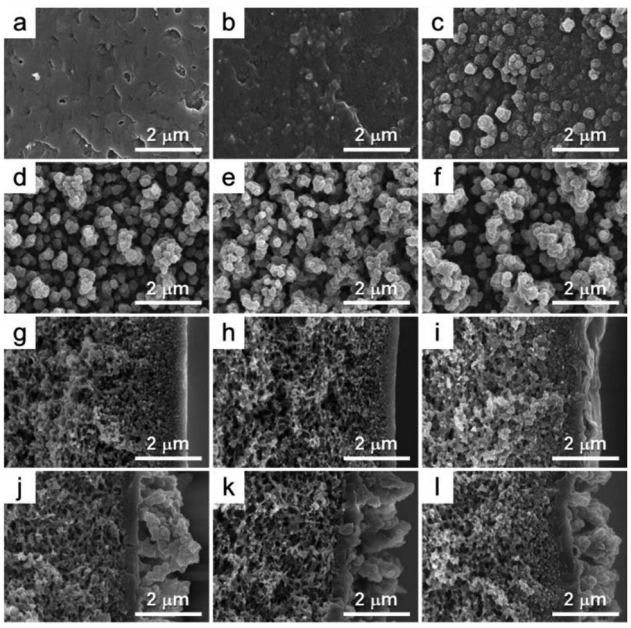

Fig. 8 Surface FE-SEM images of (a) TFC membrane and (b–f) TFN membranes with different NP-CD loading (0.1, 0.2, 0.5, 1.0, and 1.5 wt%, respectively) and cross-section images of (g) TFC membrane and (h–l) TFN membranes with different NP-CD loading (0.1, 0.2, 0.5, 1.0 and 1.5 wt%, respectively).

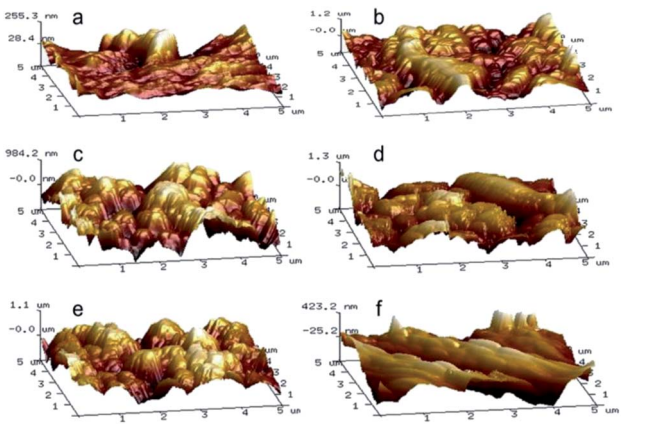

Fig. 9 Three-dimensional AFM images of (a) TFC membrane and (b–f) TFN membranes with different NP-CD loading (0.1, 0.2, 0.5, 1.0, and 1.5 wt%, respectively).

Table 2 Surface roughness parameters of TFC and TFN membranes

Membrane code	R_q (nm)	R_a (nm)	R_{max} (nm)	Relative surface area, Δ (—)
DT-TFC	56	40	247	1.07
CD-TFN(0.1)	333	273	968	2.28
CD-TFN(0.2)	348	281	1029	2.32
CD-TFN(0.5)	373	306	1069	2.38
CD-TFN(1.0)	393	318	1242	2.66
CD-TFN(1.5)	143	113	465	1.26

NP-CD particles were in the range of 1.3–3.4 nm with an average particle diameter of 2.6 nm. The surface charge of the NP-CD nanoparticles was analyzed by using the zeta potential to evaluate the stability of the nanoparticles in an aqueous suspension. Zeta potential, which is the key indicator of the surface charge of a particle, is a significant and generally utilized analysis technique and its typically estimated value of ±30 mV indicates stability of a nanomaterial. As can be seen from Fig. S2,† the zeta potential has a high absolute value (around +30 mV). It is therefore noteworthy that the NP-CD nanoparticles in deionized water have good dispersion stability, thereby resulting in the formation of a stable dispersion in DETA solution.

The functional groups of chitosan and NP-CD nanoparticles were characterized by FTIR spectroscopy and their FTIR spectra are presented in Fig. 3. The chitosan exhibits a characteristic peak at 3449 cm^{-1}, which indicates stretching oscillations of the O–H and N–H groups, and two peaks at 2927 and 2852 cm^{-1}, which attributed to the stretching oscillations of the C–H bond. There are two peaks at 1644 and 1591 cm^{-1} and a peak at 1132–1065 cm^{-1}, corresponding to the N–H bending vibrations and C–H bending vibrations, respectively. For the functionalized NP-CD nanoparticles, they show a small decrease in the absorption peak at 3439 cm^{-1} that indicates O–H and N–H stretching vibrations and a rise in the absorption peak of the amino group at 1634 cm^{-1} compared to chitosan. Additionally, the O–H (3449 cm^{-1}) and C=O (1642 cm^{-1}) vibrations confirm the presence of abundant hydrophilic groups located on the NP-CD nanoparticles. However, C–H bending vibrations of the pyranose ring at 1132–1065 cm^{-1} related to the pyranose decompose throughout application of the hydrothermal carbonization method.[33,34]

The detailed elemental composition of the NP-CD nanoparticles was further analyzed by XPS. As depicted in Fig. 4a, the XPS spectrum of the NP-CD nanoparticles exhibits five obvious elemental signals, oxygen (1s), carbon (1s), nitrogen (1s), phosphorus (2s), and phosphorus (2p). From this spectrum, it is confirmed that the NP-CDs are composed of carbon (72.3%), oxygen (21.2%), nitrogen (5.3%), and phosphorus (1.2%), which suggest that all of these elements are incorporated into the nanoparticles. In particular, the deconvolution XPS range of carbon (1s) (Fig. 4b) indicates three peaks at 283.4, 285.5, 289.5 eV, which are assigned to the C–C, C–N, and C=O groups, respectively.[35–37] In addition, the four peaks at 398.7, 399.5, 400.1, and 401.1 eV in the nitrogen (1s) spectrum (Fig. 4c) come from the N–C (sp^3), C–N–C, N–(C)3, and N–H groups, respectively.[38,39] Furthermore, the deconvoluted spectrum of oxygen (2s) is split into three peaks, at 530.4, 531.2, and 532.3 eV (Fig. 4d), which are assigned the C=O, O=C–OH, and C–OH/C–O–C groups, respectively.[35,38]

In order to investigate the optical features of the as-synthesized NP-CD nanoparticles, the UV-vis and PL spectral plots were recorded and are displayed in Fig. 5. The UV-vis absorption spectrum exhibited two characteristic absorption peaks at 293 and 340 nm, which are typically assigned to the π–π* transition of aromatic C=C, C=N, or N=P domains and the n–π* transition of conjugated C=O domains.[40–42] As shown in the PL spectrum, when excited at the maximum excitation wavelength of 365 nm, the NP-CDs showed a strong PL peak at 428 nm and strong blue fluorescence (inset in Fig. 5). The availability of carbon dots makes heteroatom doping accessible, which can effectively tune the structure of electronic energy levels and local chemical features of NP-CDs. In this manner, the electronic attributes of NP-CDs can be changed by doping with nitrogen and phosphorus particles by progressively making additional active trapping sites.[43,44] The XRD pattern in Fig. 6 shows an exceptionally polycrystalline nature and sharp peaks (2θ = 23, 32.7, 40, and 46.5°) for NP-CDs. In particular, the relatively strong diffraction peak mainly centered at 2θ = 46.7° corresponds to the graphite lattice spacing (102) plane of graphite carbon,[28,29] which is consistent with the HRTEM analysis results above. The diffraction pattern of NP-CDs prepared in this study is different from that of the previously reported patterns, which have amorphous or semi-crystalline carbon dot nanoparticles, indicating the generation of a replacement category of carbon nanomaterials, likely due to phosphorus doping.[45,46]

Characterization of TFN membranes

The ATR-FTIR spectra of the fabricated membranes are compared to the unmodified PSf substrate to identify the characteristics functional groups of interfacial polymerization

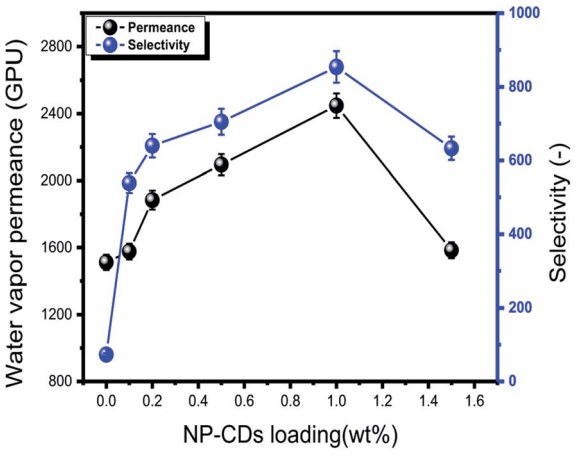

Fig. 10 The effect of the NP-CD loading on the performance of TFN membranes.

reaction. The results are presented in Fig. 7 and demonstrate that the chemical bonds and structure are available on the outside surface of the TFN layer. For the PSf support, the characteristic peaks appeared at 1586 and 1490 cm^{-1} due to the aromatic (C–C) stretching. The results also show absorption at 1152 cm^{-1} (attributed to O═S═O) and 1242 cm^{-1} (stretching vibrations of C–O–C aryl ether group); the absorption at 1295 and 1326 cm^{-1} was assigned to a doublet from the asymmetric O–S–O group. For the TFC and TFN membranes, characteristic peaks were observed at 1660 and 1548 cm^{-1} (attributed to amide I, C═O stretching and amide II, in-plane N–H bending, respectively), which are formed from the interfacial chemical reaction.[18] The peaks appeared for all the samples except PSf membrane around 3300 cm^{-1} are attributed to the OH groups which would come from the NP-CDs nanoparticles, the adsorbed OH groups surrounded the nanomaterials or from the hydrolyzed acid chloride to COOH.[47–49]

The surface morphologies of the membranes are shown in Fig. 8. From the FE-SEM images, it was observed that the NP-CD nanoparticles were well dispersed and formed a highly dense polyamide matrix on the outer surface (Fig. 8b–f). The presence of carboxylic, amino, and hydroxyl groups on the outside surface of the NP-CD nanoparticles leads to an increase their binding affinity with the polyamide matrix. Upon incorporating the nanoparticles in the TFN membranes, a dense and packed layer of a typical rough structure appeared. From the FE-SEM images, it was confirmed that the thickness of the active layer gradually increased from 270 to 1200 nm with an increment in the nanoparticle loading. Although the thickness of the nanoparticles in the polyamide layer is difficult to measure, when the nanoparticles with good affinity with the polyamide layer are introduced to the membrane surface, the overall layer thickness increases due to the effect of the nanoparticle volume.[50] The EDX data of membranes DT-TFC, CD-TFN(0.1), CD-TFN(1), and CD-TFN(1.5) are illustrated in Fig. S3.† It was observed that the membranes contains different composition of C, N, O, S, Cl with different loading content of the NP-CD nanoparticles in the TFN membranes, it shows successful incorporation of NP-CDS nanoparticles in the fabricated membranes.

The surface morphology of the TFN membranes and their roughness parameters were investigated using the AFM technique. The three-dimensional AFM images of the TFC and TFN membranes are presented in Fig. 9. The outside of the TFC layer appeared to be comparatively smooth with a 'ridge and valley' structure. With the incorporation of NP-CD nanoparticles in the DETA solution, the surface roughness increases sharply. The 'edge-valley' structure is sharp and progressively articulated, bringing about higher surface area.[51] The surface roughness parameters such as RMS (root mean square) roughness (R_q), average roughness (R_a), and maximum roughness (R_{max}) and Relative surface area are provided in Table 2. The R_q increased from 56 nm for DT-TFC to 393 nm for CD-TFN (1.0). The higher surface roughness will correspond with the larger membrane surface area, thereby resulting in higher water permeance.[52] On the other hand, loading higher than 1.0 wt% NP-CDs negatively affected the roughness because of agglomeration of the nanoparticles.

The hydrophilic nature of the membranes is critical to estimate the water vapor/N_2 separation.[22] Contact angle is one of the common methods to measure the hydrophilicity of the membranes. In this study, contact angle of PSf and TFN membranes with different loading of the NP-CD nanoparticles was measured by the sessile-drop method and is presented in Fig. S4.† The outside of the PSf substrate with a 65° contact angle was transformed in to a superhydrophilic surface after being covered with the NP-CD TFN membrane and the contact angle diminished to <9°.

Water vapor permeation study of TFN membranes

The effect of the hydrophilic NP-CD nanoparticles on the water vapor permeation for the TFN membranes was explored using the device, as illustrated in Fig. S1.† The water vapor separation performance of the TFN membranes with different NP-CD loading is presented in Fig. 10. It should be noted that pristine PSf membranes without a coating layer were not evaluated in terms of their performance because they could not be pressurized due to leaks. As the loading of the NP-CD nanoparticles was increased up to 1.0 wt%, the water vapor permeance and water vapor/N_2 selectivity of the NP-CD-incorporated polyamide membranes raised from 1511 GPU (DT-TFC) to 2448 GPU (CD-TFN(1.0)) and from 73 (DT-TFC) to 854 (CD-TFN(1.0)), respectively. This is due to the addition of NP-CD nanoparticles with many hydrophilic functional groups. Moreover, NP-CD nanoparticles provide additional vapor saturation channels to the water molecules that lead to improve in the water vapor permeation. The rise of the permeance and selectivity is attributed to the upper level of the cross-connecting network formed inside the polyamide thin skin layer, which in turn is likely a result of the imperfection free and deliquescent layer on the PSf substrate.[54] Based on the results presented in Fig. 10, it was seen that the highly packable NP-CD nanoparticles played a crucial role within the polyamide layer to create a dense and extremely packed structure that further hinder the diffusion of nitrogen molecules. Another explanation for the enhanced

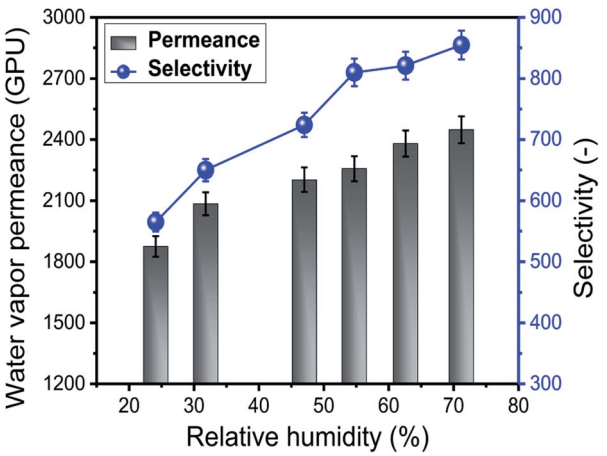

Fig. 11 The effect of RH% on the performance of the CD-TFN (1.0) membrane at 30 °C.

Table 3 Comparison of water vapor permeation with state-of-the-art composite polymeric membranes

Membrane material	Temperature (°C)	Water vapor permeance (GPU)	Selectivity	Ref.
PSf/DT-CTiO$_2$[a]	30	1340	486 [H_2O/N_2]	17
PSf/PDA/TFC[b]	30	1029	38 [H_2O/N_2]	13
PSf/MT-OH-TiO$_2$[c]	30	1396	510 [H_2O/N_2]	19
BTESO-Me-SiO$_2$[d]	40	1800	10 [H_2O/CO_2]	52
PSf/MPD-TMC-Si NPs[e]	30	2125	581 [H_2O/N_2]	18
PES/PDA/TFC[f]	30	3185	195 [H_2O/N_2]	12
DT/βCD-Fe$_3$O$_4$[g]	30	2237	774 [H_2O/N_2]	53
DT/NP-CDs[h]	30	2448	854 [H_2O/N_2]	This work

[a] TFN membrane (0.2 wt% COOH–TiO$_2$ introduced in to 1 wt% DABA and 0.2 wt% TMC). [b] Polysulfone (PSf)/PDA/thin film composite (TFC). [c] TFN membrane (0.2 wt% OH–TiO$_2$ immersed into 0.5 wt% MPD and 0.2 wt% TMC). [d] Organosilica membrane (methyl silica sols coated with bis(triethoxysilyl)octane). [e] Polysulfone (PSf)/TFC (MPD-TMC-Si). [f] Polyethersulfone (PES)-HF/PDA/TFC. [g] TFN membrane (0.2 wt% βCD-Fe$_3$O$_4$ immersed in 2 wt% DETA and 0.2 wt% TMC). [h] Thin film nanocomposite membrane (1 wt% NP-CD immersed in 2 wt% DETA and 0.2 wt% TMC).

permeance is the expansion of the surface roughness brought about by the addition of small-sized NP-CD nanoparticles, as mentioned above. The increment of the surface roughness leads to the decrement of the contact angles which interprets the outstanding deliquescent properties of the TFN membranes. Hydrophilic polar groups can bind with water molecules *via* hydrogen bonding. The NP-CD nanoparticles with many hydrophilic functional groups in TFN membranes bind with water molecules and act as active sites for water molecules, thereby resulting in higher water vapor permeance. On the other hand, after increasing the NP-CD loading up to 1.5 wt%, the water vapor permeance (1584 GPU) and selectivity (633) significantly diminished because of agglomeration, which decreased the scattering of the nanoparticles in the thin film layer.[18]

As depicted in Fig. 11, the influence of RH% on the execution of the CD-TFN (1.0) layer, which demonstrated the best permeance and selectivity, was performed at 30 °C at the steady pressure. As the RH increased in the range of 23–71%, the permeance, and the selectivity step by step inflated from 1875 to 2448 GPU and from 586 to 854, respectively. This is due to the fact that the water vapor solubilization and adsorption on the outer side of the crosslinked network are a function of its partial pressure activity.[22] The comparative outcomes and our findings are summarized in Table 3.

Conclusions

NP-CD nanoparticles with many hydrophilic functional groups were synthesized from chitosan by the one-pot green method and incorporated during interfacial polymerization, thereby resulting in dense polyamide TFN membranes. From the HRTEM images, it was confirmed that the mean particle diameter of the NP-CDs was 2.6 nm. The polyamide TFN layer on the PSf substrate provided outstanding permeance and selectivity after the addition of NP-CD nanoparticles with many hydrophilic functional groups. The enhanced membrane performance was attributed to the introduction of additional permeation pathways by the hydrophilic NP-CD nanoparticles. Due to the effect of these NP-CD nanoparticles, the CD-TFN(1.0) membrane with 1.0 wt% NP-CDs showed the best permeance (2448 GPU) and selectivity (854), which were greatly increased compared to the TFC membrane without nanoparticles (permeance (1511 GPU) and selectivity (73) for DT-TFC). These results indicate that NP-CD nanoparticles with very small size and many hydrophilic functional groups are a good candidate for membranes for water vapor separation.

Conflicts of interest

There are no conflicts to declare.

Acknowledgements

The National Research Council of Science & Technology (NST) supported this study by the Korea government (MSIP) (No. CRC-15-07-KIER).

Notes and references

1 B. C. Folkedahl, G. F. Weber and M. E. Collings, *Water extraction from coal-fired power plant flue gas*, University of North Dakota, 2006.
2 L. Jia, X. Peng, J. Sun and T. Chen, *Heat Transf. Asian Res.*, 2001, **30**, 571–580.
3 M. Strand, J. Pagels, A. Szpila, A. Gudmundsson, E. Swietlicki, M. Bohgard and M. Sanati, *Energy Fuels*, 2002, **16**, 1499–1506.
4 A. Ito, *J. Membr. Sci.*, 2000, **175**, 35–42.
5 X. Liu, Y. Zhang, K. Qu and Y. Jiang, *Energy Convers. Manage.*, 2006, **47**, 2682–2692.
6 Y. Zurigat, M. Abu-Arabi and S. Abdul-Wahab, *Energy Convers. Manage.*, 2004, **45**, 141–155.
7 F. Edwie, M. M. Teoh and T.-S. Chung, *Chem. Eng. Sci.*, 2012, **68**, 567–578.
8 M. M. Teoh and T.-S. Chung, *Sep. Purif. Technol.*, 2009, **66**, 229–236.
9 Y. Li, H. Jia, F. Pan, Z. Jiang and Q. Cheng, *J. Membr. Sci.*, 2012, **407**, 211–220.

10 G. Han, S. Zhang, X. Li, N. Widjojo and T.-S. Chung, *Chem. Eng. Sci.*, 2012, **80**, 219–231.
11 H. Sijbesma, K. Nymeijer, R. van Marwijk, R. Heijboer, J. Potreck and M. Wessling, *J. Membr. Sci.*, 2008, **313**, 263–276.
12 S. H. Yun, P. G. Ingole, K. H. Kim, W. K. Choi, J. H. Kim and H. K. Lee, *Chem. Eng. J.*, 2014, **258**, 348–356.
13 R. W. Baker and K. Lokhandwala, *Ind. Eng. Chem. Res.*, 2008, **47**, 2109–2121.
14 K. L. Wang, S. H. McCray, D. D. Newbold and E. Cussler, *J. Membr. Sci.*, 1992, **72**, 231–244.
15 X. An, P. G. Ingole, W. K. Choi, H. K. Lee, S. U. Hong and J.-D. Jeon, *J. Membr. Sci.*, 2017, **531**, 77–85.
16 P. G. Ingole, M. I. Baig, W. Choi, X. An, W. K. Choi and H. K. Lee, *J. Ind. Eng. Chem.*, 2017, **48**, 5–15.
17 M. I. Baig, P. G. Ingole, W. K. Choi, S. R. Park, E. C. Kang and H. K. Lee, *J. Membr. Sci.*, 2016, **514**, 622–635.
18 M. I. Baig, P. G. Ingole, W. K. Choi, J.-d. Jeon, B. Jang, J. H. Moon and H. K. Lee, *Chem. Eng. J.*, 2017, **308**, 27–39.
19 P. G. Ingole, M. I. Baig, W. K. Choi and H. K. Lee, *J. Mater. Chem. A*, 2016, **4**, 5592–5604.
20 G. L. Jadav and P. S. Singh, *J. Membr. Sci.*, 2009, **328**, 257–267.
21 A. Zhao, Z. Chen, C. Zhao, N. Gao, J. Ren and X. Qu, *Carbon*, 2015, **85**, 309–327.
22 M. I. Baig, P. G. Ingole, J.-d. Jeon, S. U. Hong, W. K. Choi, B. Jang and H. K. Lee, *Desalination*, 2019, **451**, 59–71.
23 J. Zhang and S.-H. Yu, *Mater. Today*, 2016, **19**, 382–393.
24 X. Li, M. Rui, J. Song, Z. Shen and H. Zeng, *Adv. Funct. Mater.*, 2015, **25**, 4929–4947.
25 C. Zhang, K. Wei, W. Zhang, Y. Bai, Y. Sun and J. Gu, *ACS Appl. Mater. Interfaces*, 2017, **9**, 11082–11094.
26 Y. Li, S. Li and K. Zhang, *J. Membr. Sci.*, 2017, **537**, 42–53.
27 Y. Huang, Y. Liang, Y. Rao, D. Zhu, J.-j. Cao, Z. Shen, W. Ho and S. C. Lee, *Environ. Sci. Technol.*, 2017, **51**, 2924–2933.
28 B. Shi, Y. Su, L. Zhang, M. Huang, R. Liu and S. Zhao, *ACS Appl. Mater. Interfaces*, 2016, **8**, 10717–10725.
29 W. Lu, X. Qin, S. Liu, G. Chang, Y. Zhang, Y. Luo, A. M. Asiri, A. O. Al-Youbi and X. Sun, *Anal. Chem.*, 2012, **84**, 5351–5357.
30 Y. Yang, J. Cui, M. Zheng, C. Hu, S. Tan, Y. Xiao, Q. Yang and Y. Liu, *Chem. Commun.*, 2012, **48**, 380–382.
31 W. Wang, Y.-C. Lu, H. Huang, J.-J. Feng, J.-R. Chen and A.-J. Wang, *Analyst*, 2014, **139**, 1692–1696.
32 S. Liu, J. Tian, L. Wang, Y. Luo, J. Zhai and X. Sun, *J. Mater. Chem.*, 2011, **21**, 11726–11729.
33 S. Liu, J. Tian, L. Wang, Y. Luo and X. Sun, *RSC Adv.*, 2012, **2**, 411–413.
34 S. K. Bhunia, A. Saha, A. R. Maity, S. C. Ray and N. R. Jana, *Sci. Rep.*, 2013, **3**, 1473.
35 X. Sun, C. Brückner and Y. Lei, *Nanoscale*, 2015, **7**, 17278–17282.
36 Q. Xiao, Y. Liang, F. Zhu, S. Lu and S. Huang, *Microchim. Acta*, 2017, **184**, 2429–2438.
37 M. Xue, L. Zhang, Z. Zhan, M. Zou, Y. Huang and S. Zhao, *Talanta*, 2016, **150**, 324–330.
38 P. Roy, P.-C. Chen, A. P. Periasamy, Y.-N. Chen and H.-T. Chang, *Mater. Today*, 2015, **18**, 447–458.
39 S. Zhu, J. Zhang, S. Tang, C. Qiao, L. Wang, H. Wang, X. Liu, B. Li, Y. Li and W. Yu, *Adv. Funct. Mater.*, 2012, **22**, 4732–4740.
40 Y. Yan, H. Yang, F. Zhang, B. Tu and D. Zhao, *Carbon*, 2007, **45**, 2209–2216.
41 H. Zhu, X. Wang, Y. Li, Z. Wang, F. Yang and X. Yang, *Chem. Commun.*, 2009, 5118–5120.
42 B. Mohanty, A. K. Verma, P. Claesson and H. Bohidar, *Nanotechnology*, 2007, **18**, 445102.
43 B. J. A. Tarboush, D. Rana, T. Matsuura, H. Arafat and R. Narbaitz, *J. Membr. Sci.*, 2008, **325**, 166–175.
44 H. Shawky, S.-R. Chae, S. Lin and M. Wiesner, *Synthesis and characterization of a carbon nanotube/polymer nanocomposite membrane for water treatment*, 2011.
45 H. S. Lee, S. J. Im, J. H. Kim, H. J. Kim, J. P. Kim and B. R. Min, *Desalination*, 2008, **219**, 48–56.
46 Z. Lu, X. Qi, Z. Zhang, D. Yang, Q. Gao, Y. Jiang, X. Xiong and X. Y. Liu, *Cryst. Growth Des.*, 2016, **16**, 4620–4626.
47 P. G. Ingole, W. Choi, K.-H. Kim, H.-D. Jo, W.-K. Choi, J.-S. Park and H.-K. Lee, *Desalination*, 2014, **345**, 136–145.
48 F. Pan, H. Jia, Z. Jiang and X. Zheng, *J. Membr. Sci.*, 2008, **325**, 727–734.
49 J. Yin, E.-S. Kim, J. Yang and B. Deng, *J. Membr. Sci.*, 2012, **423**, 238–246.
50 Z.-Q. Xu, L.-Y. Yang, X.-Y. Fan, J.-C. Jin, J. Mei, W. Peng, F.-L. Jiang, Q. Xiao and Y. Liu, *Carbon*, 2014, **66**, 351–360.
51 H. Li, H. Ming, Y. Liu, H. Yu, X. He, H. Huang, K. Pan, Z. Kang and S.-T. Lee, *New J. Chem.*, 2011, **35**, 2666–2670.
52 X. Ren, M. Kanezashi, H. Nagasawa and T. Tsuru, *J. Membr. Sci.*, 2015, **496**, 156–164.
53 A. M. Abou-Elanwar, Y. M. Shirke, P. G. Ingole, W.-K. Choi, H. Lee, S. U. Hong, H. K. Lee and J.-D. Jeon, *J. Mater. Chem. A*, 2018, **6**, 24569–24579.
54 P. G. Ingole, W. K. Choi, I.-H. Baek and H. K. Lee, *RSC Adv.*, 2015, **5**, 78950–78957.